www.advelectronicmat.de

# Resolving the Relaxation of Volatile Valence Change Memory

Johannes Hellwig,\* Carsten Funck, Sebastian Siegel, Alexandros Sarantopoulos, Dimitrios Spithouris, Stephan Menzel, and Regina Dittmann

Memristive devices based on the valence change mechanism are highly interesting candidates for data storage and hardware implementation of synapses in neuromorphic circuits. Although long-term retention is often required for data storage applications, a slight resistance drift of the low resistive state (LRS) is observed even for stable devices. For other devices, the LRS has been observed to decay rapidly to the high resistive state (HRS). These types of devices are of interest for neuromorphic circuits where short-term plasticity is required. In this work, the LRS relaxation of volatile, crystalline Pt/SrTiO<sub>3</sub>/Nb:SrTiO<sub>3</sub>: devices is investigated in detail, yielding time constants ranging from milliseconds to seconds. The decay is analyzed in terms of the Gibbs free energy gradient for the contribution of oxygen ion migration. A relaxation model based on drift-diffusion dynamics is presented. The model may serve as a tool for developing guidelines and design rules for future volatile memristive technology based on Schottky barrier mediated electron transport.

#### 1. Introduction

Neuromorphic hardware aims to mimic the functionality of the human brain and sensory processing system in electronic circuits and systems. [1] A candidate for the implementation of artificial neurons and synapses are memristive devices. [2–4] These are electrical resistors with an electrically tuneable resistance. They are being investigated as an emerging kind of data storage device with low energy and silicon area consumption, and are now being used as embedded memory on industrial level. [5,6] For use in artificial synapses and neurons, memristive devices with both nonvolatile or volatile behavior can be employed. [1,7]

While nonvolatile devices can be used to store static synaptic weights, in contrast, the relaxation of a volatile device has strong similarities to the forgetting process in the human brain,

J. Hellwig, C. Funck, S. Siegel, A. Sarantopoulos, D. Spithouris, S. Menzel, R. Dittmann
Forschungszentrum Jülich Gmbh PGI-7 & JARA-FIT
52428 Jülich, Germany
E-mail: j.hellwig@fz-juelich.de



The ORCID identification number(s) for the author(s) of this article can be found under https://doi.org/10.1002/aelm.202400062

© 2024 The Author(s). Advanced Electronic Materials published by Wiley-VCH GmbH. This is an open access article under the terms of the Creative Commons Attribution License, which permits use, distribution and reproduction in any medium, provided the original work is properly cited.

DOI: 10.1002/aelm.202400062

where an initial sharp loss of information evolves into a long-tail relaxation. [8] In conventional CMOS technology, the fading of information is achieved using capacitors. However, the capacitance of CMOS capacitors scales with their area, so time scales are limited. Volatile memristive devices based on the valence change mechanism (VCM) fill this gap. They exhibit high switching speed, gradual switching, low power consumption, a possible nm² footprint, and engineerable decay time constants in the range of seconds to fit a specific neuromorphic time domain. [9]

To develop design rules for effectively tuning the time constants of the devices, knowledge of the physical origin of the decay is required. In addition, a (physical) model is needed to enable simulation and design of neuromorphic computing

systems. A physical decay model, however, for valence change mechanism (VCM)-based devices has not yet been reported.

Pt/SrTiO<sub>3</sub>(STO)/Nb:STO devices are often used as a model system for VCM resistive switching where oxygen vacancies act as shallow donors, also known as "type 1" conduction system in literature.<sup>[10]</sup> For this work, the system is chosen due to the deep understanding of the electron conduction process and the existing knowledge of the defect chemistry and oxygen diffusion during the switching process.<sup>[11–14]</sup> In addition, the engineering of the device retention time has been demonstrated.<sup>[15]</sup> In the study mentioned, the focus is on long retention times, which are important for data storage, in-memory computing, and neural networks. There is a lack of research on the engineering of short retention times, however, they may be applied, for example, in time-of-flight measurement circuits such as the Time Difference Encoder (TDE).<sup>[16]</sup>

In type 1 memristive devices, such as STO devices, the electrical resistance is determined by a Schottky barrier, here at the Pt/STO interface, and electron transport takes place in the conduction band. [10,13] In eightwise (8w) polarity, i.e., when the device is switched from a high-resistive state (HRS) to a low-resistive state (LRS) with a positive voltage applied to the Pt electrode, Pt/STO/Nb:STO devices exhibit bipolar switching. This is due to the modulation of oxygen vacancies within a filament in the vicinity of the Pt electrode. It has been found that oxygen vacancies are created within the STO and that the released oxygen accumulates at the Pt electrode during the SET process. Oxygen is incorporated into the Pt metal and/or released in gaseous form. [17] When the voltage is reversed, oxygen from the



www.advelectronicmat.de

surrounding atmosphere and the oxygen stored in the Pt electrode recombine with the oxygen vacancies, increasing the width of the Schottky barrier and reducing the tunnel current.

For STO, retention time constants of minutes, days, or even years have been observed for different stoichiometries and interface configurations.[18] Previously, Bäumer et al. showed that the decay is caused by the reoxidation of the filament and that retention can be drastically improved by incorporating oxygen blocking layers at the Pt/STO interface.[18] Similarly, it has been demonstrated that in non-stoichiometric, Sr-rich STO cells (Sr/(Sr+Ti) ≈0.52), oxygen-blocking SrO forms at the interface, resulting in a longer retention time than in stoichiometric cells.<sup>[19]</sup> Furthermore, an ionic origin is supported by several studies investigating the influence of the top electrode. [20,21] However, the oxygen exchange with the electrode and the atmosphere is also determined by the particular biasing conditions, such as the current compliance used during switching.<sup>[20]</sup> This may also be related to the size of the filament and the penetration of oxygen into the electrode. In addition to device engineering, retention is also dependent on the ambient atmosphere, as this is likely to affect the oxygen supply for reoxidation. The retention time of cells operated under vacuum conditions is drastically increased.<sup>[15]</sup> DFT studies suggest that the actual reincorporation of oxygen into STO probably occurs in microseconds.[22]

These considerations support the idea that the decay is governed by the reincorporation of oxygen into STO and that it can be controlled by engineering the oxygen migration. However, the relaxation measurements found in the literature often lack a full physical description (physical model) or are only vaguely explained by electronic trapping and detrapping and/or ionic processes. They are described by multiple exponential functions, [23,24] stretched exponential functions, [8,25] a power law, or a combination of both.[26,27] In some reports, resistive switching in STO cells has been attributed to trapping and detrapping of electrons in the interfacial layer. [28,29] As a result, the relaxation was explained by a purely electronic process.<sup>[24,30]</sup> Others present decays of VCM cells with multiple time constants in the second range suggesting that the decay is a combination of electronic and ionic behavior.[27] Interestingly, in these studies the longer time constant is often attributed to an electronic process. Purely ionic explanations with decay time constants from 40 ms to 500 s can also be found.[2,31]

This work aims to identify the origin of the relaxation of filamentary, type 1 VCM-devices. We present detailed studies of the LRS decay process in single crystalline Pt/STO/Nb:STO devices. As in the literature, the decays exhibit at least two time constants; a fast decay immediately after the pulse in the millisecond regime and a long-term relaxation in the second regime. Using the oxygen vacancy configuration in the filament region from our previous work,[32] and the Tsu-Esaki formalism, we can estimate the charge density at the interface from the measured current density for each point in time. By applying the concept of the Gibbs free energy to our measurements, we show that both time constants can best be attributed to ionic migration near the Pt/STO and to the oxygen exchange at this interface. We propose an ionic model to explain long- and short-term relaxation. This is intended to clarify the confusion surrounding the relaxation of filamentary, type 1 memristive devices. Our model may aid in the develop-

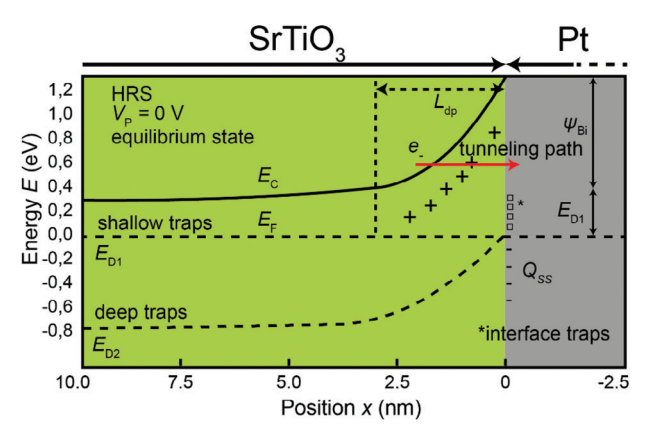


**Figure 1.** The band diagram of the Nb:STO/STO/Pt devices without applied voltage. The device is in the equilibrium HRS corresponding to a specific depletion zone width  $L_{\rm dp}$ . The image is a reproduction from Bäumer et al. [33]

ment of guidelines and design rules for future volatile memristive technology.

## 2. Basic Current Transport Model

It has been shown that electron tunneling through the Schottky barrier at the Pt/STO interface determines the current transport through the devices. [10,13] The band diagram at this interface is shown in (**Figure 1**). The figure shows two in-gap states,  $E_{\rm D1}$  and  $E_{\rm D2}$ , below the conduction band. Their ionization energies have been spectroscopically identified for STO as 0.3 eV and 1.1 eV for single and double charged oxygen vacancies, respectively. [33] Within the depletion zone, the shallow trap level is vacant and screens the surface charge. In contrast, the deep traps are located below the Fermi level and are permanently occupied by trapped electrons. In the device stack, further traps can arise from surface states above the Fermi level. [34]

Using the Poisson equation in depletion approximation, this electrical potential  $\phi(x)$  at the interface for a position x within the depletion zone can be defined as shown in Equation (1) for a basic Schottky contact:<sup>[35]</sup>

$$\phi(x) = -\frac{eN}{2\varepsilon_r \varepsilon_0} L_{dp}^2 \left( 1 - \frac{x}{L_{dp}} \right)^2$$
 (1)

here, e denotes the elementary charge,  $e_r$  the relative dielectric permittivity of STO,  $e_0$  the vacuum permittivity, and N the density of single positively charged oxygen vacancies, which we approximate to be homogenous within the depletion region for each timestep.  $L_{\rm dp}$  is the depletion zone width as shown in Figure 1.

Although this assumption contrasts with our experiments where a gradient in vacancy concentration is observed, [17] it drastically reduces the complexity of the model and was already applied successfully in earlier studies. [13] A simulation of the non-homogeneous vacancy concentration would need to account for the complex electro-chemical equilibrium at the interface and would exceed the scope of this work.

 $L_{
m dp}$  is the depletion zone width as shown in Figure 1. The position x=0 refers to the STO/Pt interface. From the electrostatic



www.advelectronicmat.de

potential, the energy of the conduction band edge can be calculated (see Figure 1a):

$$E_c(x) = -e\phi(x, V) + E_{D1}$$
 (2)

Here,  $E_{\rm D1}$  is the energy of the shallow trap, which displays the Fermi level. The interface potential in Equation (1) has its maximum value  $\phi_{\rm d}$  at x=0:[35]

$$\phi_{\rm d} = \left(\phi_{\rm i} - \phi\right) = -\frac{eN}{2\epsilon_{\rm r}\epsilon_{\rm 0}} L_{\rm dp}^2 \tag{3}$$

 $\phi_i$  is the internal potential and  $\phi$  is an external applied potential. We define the built-in energy  $\psi_{\rm Bi}$  as:

$$\psi_{\rm Bi} = -e\phi_{\rm d} \tag{4}$$

The length of the depletion zone  $L_{\rm dp}$  that defines the Schottky barrier is given by:<sup>[35]</sup>

$$L_{\rm dp} (V) = \sqrt{\frac{2\varepsilon_r \varepsilon_0 \psi_{\rm Bi}}{e^2 N}}$$
 (5)

Previous studies have shown that electrons are injected into the device by a tunneling process through this Schottky barrier. This can be quantified using the Tsu–Esaki formalism combined with the Wentzel–Kramers–Brillouin (WKB) approximation.<sup>[36–38]</sup> Following Marchewka et al.,<sup>[37]</sup> the resulting current density can be written as

$$j_{\text{tunnel}} = \frac{4\pi e}{h^3} \int_{E_{\text{DL}}}^{E_{\text{C}}(x=0)} N_{\text{sup}} \left( E, E_{f,\text{Pt}}, E_{f,\text{STO}}, T \right) Tr \left( E \right) dE$$
 (6)

Here, T denotes the temperature, Tr(E) is the transmission probability through the barrier at energy E, and  $N_{\sup}(E, E_{f,Pt}, E_{f,STO}, T)$  is the supply function. The former is derived from the WKB approximation. [13,37] It is given by:

$$Tr (E) = \exp\left(-\sqrt{\frac{8m}{\hbar^2}} \int_{x(E_c)}^{L_{dp}} \sqrt{E - E_c(x)} dE\right)$$
 (7)

Here, m is the electron mass. Tr(E) depends on the width of the depletion zone, which is given by Equation (5).

The supply function  $N_{\text{sup}}$  describes the sites available for tunneling at a given specific energy:<sup>[38]</sup>

$$N_{\text{sup}}\left(E, E_{f,\text{Pt}}, E_{f,\text{STO}}, T\right) = k_b T \ln \left(\frac{1 + \exp\left(-\frac{E - E_{f,\text{STO}}}{k_b T}\right)}{1 + \exp\left(-\frac{E - E_{f,\text{Pt}}}{k_b T}\right)}\right)$$
(8)

Here,  $E_{f,STO}$  is the Fermi-level of the STO, which is fixed to 0 eV in this work.  $E_{f,Pt}$  is the Fermi-level of the Pt, which depends on the external applied potential φ:

$$E_{f,Pt} = -e\phi \tag{9}$$

To calculate the current density, in Equation (6), the supply function and the transmission probability are integrated over all energy states from the Fermi level at  $E_{\rm D1}$  to the barrier maximum

 $E_{\rm C}(x=0)$ . The total current through the device equals the current density  $j_{\rm tunnel}$  multiplied by the area A of the filament. We assume that the filament is circular with an area of  $A=\pi r_{\rm filament}^2$ , and a radius of  $r_{\rm filament}$ .

Since the tunneling current through the device strongly depends on the width of the depletion region, changing the electronic configuration at the interface has a strong effect on the resistance of the device. Injection of charge into the depletion region changes its width, as shown in Equation (5), which, in turn, affects the transmission probability of electrons, see Equation (7). In the case of negative charges, the depletion width is increased, which reduces the tunneling current. The opposite is true for positive charges. An LRS is established when positively charged oxygen vacancies are attracted to the Schottky barrier, whereas an HRS is established when the interfacial region is depleted of oxygen vacancies. Barrier modulation can also be induced by electrons trapped at or emitted from defect states within the depletion zone.

## 3. Ionic Decay Model

Figure 2a shows the Pt/STO/Nb:STO device structure used in this work. The currents are measured using a measurement sequence as shown in Figure 2b. Prior to measurement, the device is set to an HRS of 100 M $\Omega$ . The sequence starts with a readout followed by the SET pulse  $V_{\rm p}$  using a rise and fall time of 0.1 ms and a specific hold time  $t_p$  at  $V_p$ . Directly after the SET pulse, we apply a 0.3 V DC type readout for 16 s. Figure 2c shows a decay measurement over 16 s measured at 0.3 V. In simple terms, the readout follows a combination of at least three exponential functions with time constants  $\tau_1$ ,  $\tau_2$ , and  $\tau_3$ , where  $\tau_1$  is  $\approx 0.040$  s and  $\tau_2$  is  $\approx 0.58$  s, and  $\tau_3 \approx 2.44$  s (The fittings can be found in the supplementary information). Figure 2d shows three sequences for different SET pulse voltages. At 3 V the current reaches the compliances of 3 mA. An example readout period of 100 ms is depicted. When the voltage level is changed, the system shows capacitive charging spikes at the beginning of the sequence and after the readout period. Figure 2e shows the current-voltage curve of a Pt/STO/Nb:STO device. The device is switched to the LRS and HRS by applying a positive or negative voltage to the Pt electrode, respectively. As shown in Figure 2a, the voltage is applied to the top electrode. The Nb:STO bottom electrode is grounded. During the initial switching of the cell, it exhibits an electroforming step.

Our previous studies referenced in the introduction could identify oxygen release and reincorporation as switching mechanism.<sup>[17,32,39]</sup> They also strongly suggest an ionic origin for the decay since it can be prevented by measuring in vacuum.<sup>[15]</sup> Further, we exclude electronic effects for the origin of the decay for two reasons. Electron trapping/emission may arise from interface traps, or traps located within the depletion zone.<sup>[40]</sup> After the SET event of the device to the LRS, these traps are filled and emit electrons into the conduction band.<sup>[34]</sup> Electron emission shrinks the barrier, which increases the tunneling current. Additionally, emission currents are in the opposite direction to the tunneling current and have time constants smaller than the observed decay time constants in the experiments. Related calculations and considerations about electron capture and emission processes can be found in the



www.advelectronicmat.de

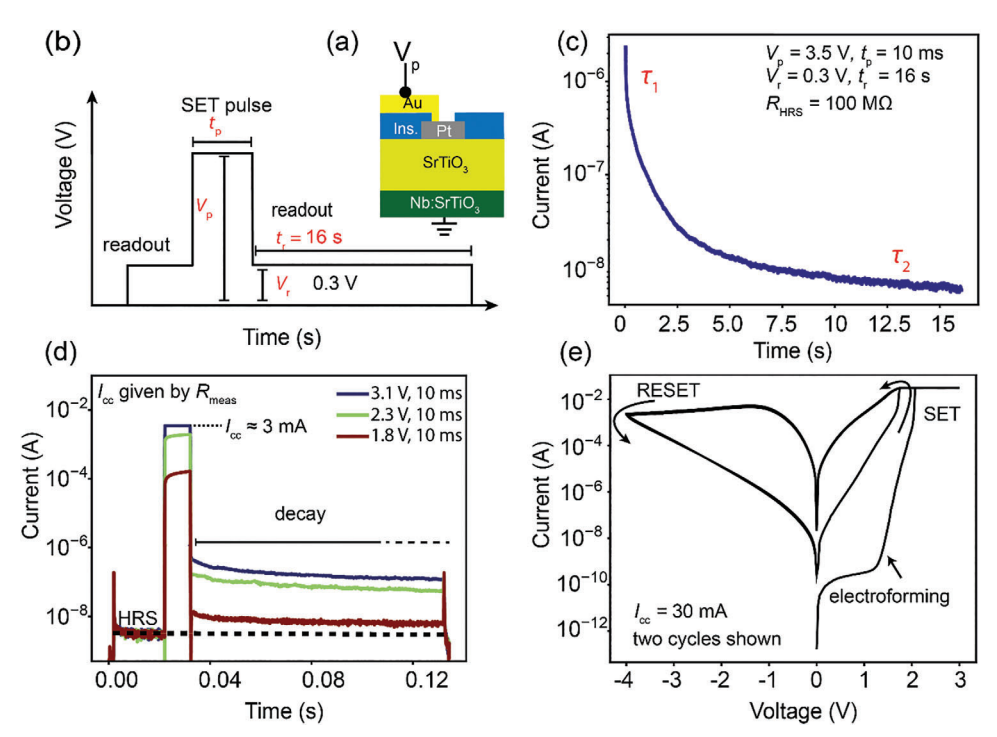


Figure 2. Resistive switching of and retention measurement on a Pt/STO/Nb:STO device. a) The stack of the Pt/STO/Nb:STO device. The voltage is applied to the Pt top electrode using b) a specific decay measurement sequence. c) Current decay measurement during the readout period of 16 s at 0.3 V. d) Current response of the device for three different SET pulse voltages with a readout period of 100 ms after the SET pulse. The current is measured via a resistor which limits the maximum current to 3 mA. e) Exemplary current—voltage sweep measured using a current compliance of 30 mA.

supporting information. Instead, we propose an ionic decay model, based on the ionic exchange at the Pt/STO interface and ionic motion at the vicinity of this interface. We assume a transient reoxidation of the interfacial region, which is modeled as a transient change in the oxygen vacancy concentration within the depletion zone. The latter is mediated by multiple migration barriers at the Pt interface and within the STO. We use the Tsu-Esaki framework to translate this transient oxygen vacancy concentration into current density within the device.

Electrochemically, the interface reaction is an oxygen evolution and reduction reaction.[12] Merkle et al. show that this is a complex process that is rate-limited by an electron transfer process. [41] To incorporate oxygen from the STO into the Pt electrode, density functional theory (DFT) simulations by Zurhelle et al. show energies between 2.66 and 3.79 eV.[42] This process is promoted by the presence of extended defects, such as dislocations and grain boundaries. It can even be prevented, as shown by Mikheev et al., for an epitaxially grown, Pt electrode. [26] To reincorporate oxygen into the STO, smaller activation energies between 0.16 and 0.86 eV were calculated.[22] It has been found that oxygen is exchanged between the STO layer and the surrounding atmosphere. This exchange may be mediated by grain boundary migration inside the Pt electrode<sup>[39,42]</sup> Within the bulk STO, oxygen ions migrate via oxygen vacancies. Therefore, the movement of oxygen vacancies is in the opposite direction to that of the oxygen ions. This movement is governed by an ion hopping process. Here, the equilibrium oxygen migration barrier varies between  $0.6 \text{ and } > 1 \text{ eV}.^{[43]}$ 

We propose that the driving force for the observed decay behavior is the gradient in chemical potential that is created during the accumulation of oxygen vacancies at the vicinity of the Pt electrode during the SET pulse. We define the decay as the relaxation of this gradient and the resistive states of the device as stable/unstable states in Gibbs free energy. In our model, the HRS of the device is treated as an internal equilibrium at the readout voltage with a certain oxygen vacancy concentration  $N_{HRS}$ . During the SET process, the device is pushed out of this equilibrium by the incorporation of oxygen into the Pt electrode. This increases the concentration of oxygen vacancies at the interface resulting in a decrease in the Gibbs energy  $\Delta G$  with respect to the Pt electrode and the bulk. This is the driving force for the migration of oxygen ions/vacancies leading to a relaxation of the cell toward the equilibrium HRS. The duration of the whole process determines the retention of the device, while the depletion zone determines the current transport of the device.

In our model, the depletion zone is the region of interest. We model it as a container of oxygen vacancies that can exchange oxygen with the  $SrTiO_{3-x}$  bulk and the Pt metal electrode. For simplicity, it is divided into three sublayers. A sketch of the different layers in the simulation model is shown in **Figure 3**. The first describes the first atomic layer of  $SrTiO_{3-x}$  at the Pt interface. We call it the recombination layer R since it mediates the oxygen exchange with the Pt metal electrode M. The second is defined as the supply layer S. It covers the second slab of the depletion zone and couples to the bulk STO layer B via the transition region T. The transition region T usually contains more than one unit cell, but for simplicity it is modeled as one container. The

conditions) on Wiley Online Library for rules of use; OA articles are governed by the applicable Creative Commons

www.advelectronicmat.de

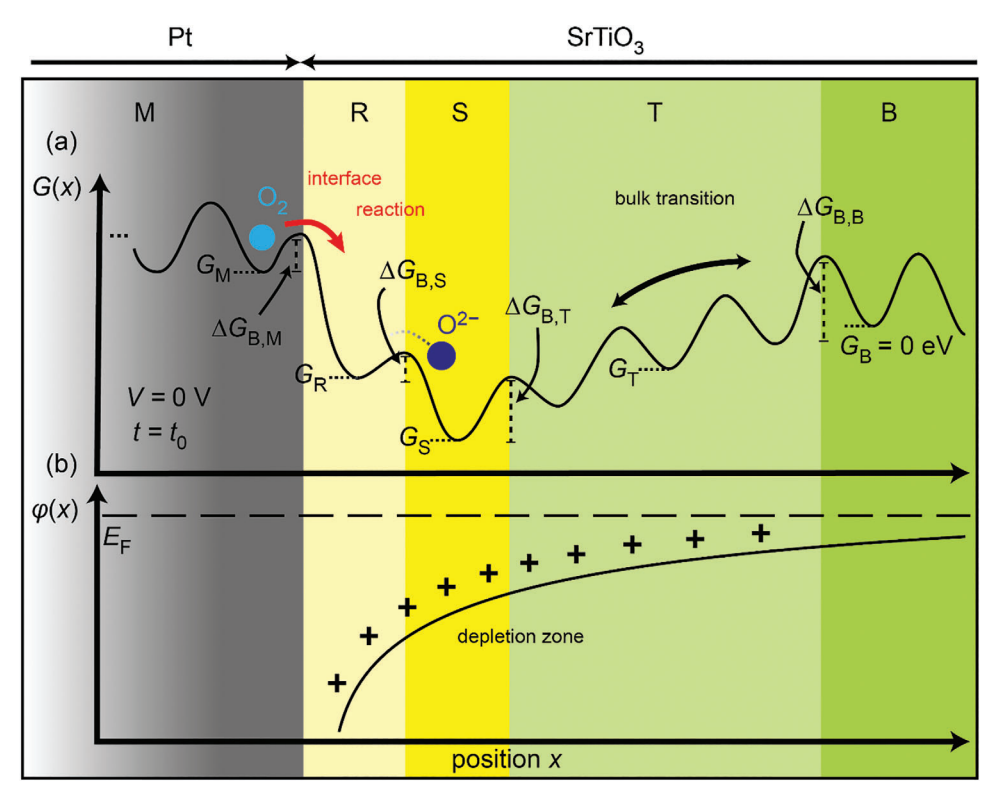


Figure 3. The ionic hopping model and the local Gibbs free energy of oxygen. a) The oxide is divided into five regions as shown at the top: the metal M, the recombination region R directly at the interface, the supply region S, the transition region T, and the bulk B. Each region has a Gibbs free energy G and can exchange oxygen with the other regions via an oxygen migration barrier  $\Delta G_{B,i}$ . The movement of oxygen during the decay is shown. Within the Pt oxygen is most likely stored as molecular oxygen  $O_2$  at grain boundaries. At the interface  $O_2$  molecules undergo an interface reaction to  $O^2$ . Oxygen ions within the STO migrate via oxygen vacancies  $V_O^*$  (not shown). b) The interface potential affects the interface exchange and the near interface ion migration.

coupling between each adjacent region is provided by an oxygen migration barrier  $G_{B,i}(i = \{M,R,S,B\})$ . These barriers are lowered or raised by changing the local Gibbs energy due to variations in electrical potential (e.g., an externally applied voltage) or in the oxygen vacancy concentration.

At the interface the Gibbs free energy is dominated by the electro-chemical potential arising from the depletion zone. [44] The internal electrical energy is given by the built-in energy at the interface which decreases parabolically in the depletion zone. In contrast to an electron in the conduction band, oxygen is doubly negatively charged and has no offset  $E_{\rm D1}$ . Using Equation (1) and considering the double negative charge of the oxygen ions, the oxygen energy is given by

$$E_{\text{Ox}}(x, V, N) = 2 \cdot \psi_{\text{Bi}} \cdot \left(1 - \frac{x}{L_{\text{dp}}(V, N)}\right)^2$$
 (10)

It is assumed that the interface is at x=0. At a read voltage  $V_{\rm Read}$  and an HRS concentration  $N_{\rm HRS}$ , the equilibrium energy is calculated by  $E_{\rm Ox,eq}(x, V_{\rm Read}, N_{\rm HRS})$ . In this quasi-equilibrium state, there is no net flux between the three ranges, R, S, T, and the metal M and the bulk B. This allows to define the gradient in electro-chemical energy  $\Delta G$  as the difference of the oxygen energies: [45]

$$\Delta G(x, V, N) = E_{Ox}(x, V, N) - E_{Ox,eq}(x, V, N_{HRS})$$
 (11)

Here, V is the applied readout voltage and N the average oxygen vacancy concentration inside the depletion zone. The average oxygen vacancy concentration within the depletion zone is the average concentration of the three layers:

$$N = \frac{1}{2 + \alpha} \left( N_{\rm R} + N_{\rm S} + \alpha N_{\rm T} \right) \tag{12}$$

The transition region T extends over more than one unit cell. Therefore, the factor  $\alpha$  is introduced in Equation  $N_{\rm T}$ , which is the average number of unit cells covered by T. Using Equation (11), it is possible to calculate the local Gibbs energy for the metal, the R, S, and T layers and the bulk. The reference Gibbs energy is set to the layer/bulk  $G_{\rm Bulk}=0$  eV. The Gibbs energy in each region is given by

$$G(x, V, N) = G_{\text{Bulk}} + \Delta G(x, V, N)$$
(13)

In equilibrium, the Gibbs energy is equal to the bulk value and  $\Delta G$  is zero. However, the  $\operatorname{SrTiO}_{3-x}$  is not in total equilibrium with the environment and the Gibbs energy in the metal  $G_{\mathrm{M}}$  is increased by  $G_0$  from the bulk reference ( $G_0 \neq G_{\mathrm{B}}$ ). The recombination region is described by the first atomic layer which allows oxygen transfer to the metal. As a conclusion, the position of R is set to  $x=0.5a_{\mathrm{STO}}$ , where  $a_{\mathrm{STO}}$  is the unit cell length of STO.

2199160x, 2024, 12, Downloaded from https://onlinelibrary.wiley.c

com/doi/10.1002/aclm.202400062 by Forschungszentrum Jülich GmbH Research Center, Wiley Online Library on [18/12/2024]. See the Terms

conditions) on Wiley Online Library for rules of use; OA articles are governed by the applicable Creative Commons

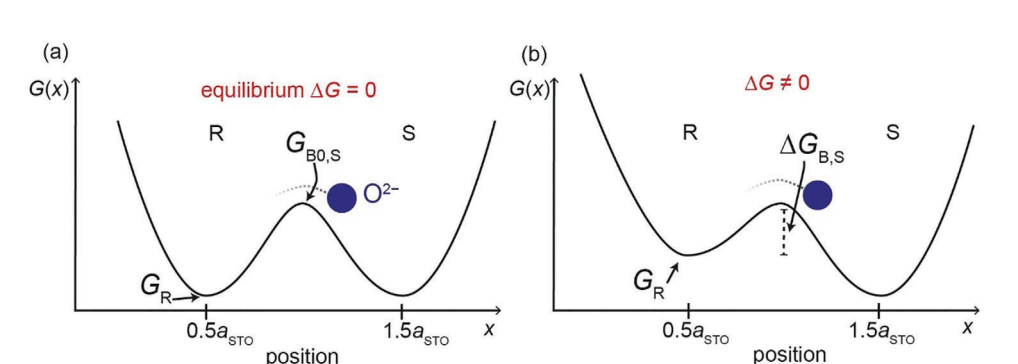


Figure 4. The ionic hopping mechanism for a hop from lattice site R to S for oxygen ions. The oxygen vacancy ion movement is in the opposite direction. a) The equilibrium case. The saddle point is at  $G_{B0,S}$ . b) The non-equilibrium case where a gradient in Gibbs free energy,  $\Delta G \neq 0$ , is superimposed on the energy landscape. The energy  $G_{B0,S}$  is lowered to  $G_{B,S}$  by  $\Delta G$ . The effective migration barrier is then given by  $\Delta G_{B,S}$  as it depends on the energy at  $G_{B,S}$  as it depends on the energy at  $G_{B,S}$  and  $G_{B,S}$  are in the energy at  $G_{B,S}$  and  $G_{B,S}$  are in the energy  $G_{B,S}$  and  $G_{B,S}$  are in the energy at  $G_{B,S}$  and  $G_{B,S}$  are in the energy  $G_{B,S$ 

The supply range S is one lattice point away, so at  $x = 1.5a_{STO}$ . This leads to the Gibbs energies at the different positions:

$$G_{\rm M}(V) = G_0 \tag{14}$$

$$G_{\rm T}(V, N) = G_{\rm Bulk} + \Delta G(2.5a_{\rm STO}, V, N)$$
 (15)

$$G_{\rm S}(V, N) = G_{\rm Bulk} + \Delta G(1.5a_{\rm STO}, V, N)$$
 (16)

$$G_{R}(V, N) = G_{Bulk} + \Delta G(0.5a_{STO}, V, N)$$
(17)

$$G_{\rm B}(V,N) = G_{\rm Bulk} \tag{18}$$

In Equations (15)–(17) each energy depends on the average concentration N and not on the specific concentration, see Equation (12).

Diffusion and migration processes inside a crystal lattice are governed by an ionic hopping mechanism between lattice positions, which is commonly described by the Mott–Gurney law. [46–48] The interface reaction is an oxygen evolution reaction and is described using the Butler–Volmer equation. [48] With no voltage applied both are mathematically equivalent and define a migration process across an energy barrier by considering the forward and backward motion. Following De Souza et al., this hopping process is a thermally excited process and can be approximated as the jump rate  $R_{\rm AB}$  from a lattice site A to B:[11]

$$R_{\rm AB} = v_{\rm Ph} \exp\left(-\frac{G_{\rm B,AB}\left(V,N\right) - G_{\rm A}\left(V,N\right)}{k_{\rm B}T}\right) \tag{19}$$

Here,  $v_{\rm Ph}$  denotes the attempt frequency which is given by the phonon frequency of the lattice.  $G_{\rm B,AB}(V,N)$  is the maximum free energy (saddle point energy) on the migration path between the two ranges, here A and B.

The barrier is lowered by the Gibbs free energy at lattice site  $G_{\rm A}$ . The position of the migration barrier to the metal is given by x=0, whereas the barrier between S and R is located at  $x=a_{\rm STO}$ . The last contact to the bulk environment is given at the end of the depletion zone  $x=L_{\rm dp}$  (V). In addition, the migration barriers are modulated by  $\Delta G$  depending on their location within the depletion zone. The saddle point energies  $G_{\rm B,M}$ ,  $G_{\rm B,S}$ ,  $G_{\rm B,T}$ , and  $G_{\rm B,B}$  of the transition barriers for the metal, the supply layer,

the transition region and the bulk are given by Equations (20)–(23):

$$G_{\rm BM}(V, N) = G_{\rm R0M} + \Delta G(0, V, N)$$
 (20)

$$G_{\text{B.S.}}(V, N) = G_{\text{B0.S.}} + \Delta G(a_{\text{STO}}, V, N)$$
 (21)

$$G_{\rm B,T}(V,N) = G_{\rm B0,T} + \Delta G(2a_{\rm STO}, V, N)$$
 (22)

$$G_{\text{RR}}(V, N) = G_{\text{ROR}} + \Delta G(L_{\text{DR}}(V), V, N).$$
 (23)

where  $G_{\rm B0,M}$ ,  $G_{\rm B0,S}$ ,  $G_{\rm B0,T}$ , and  $G_{\rm B0,a}$  are the (equilibrium) migration saddle points of the respective transition paths. Equation (23) is the saddle point that connects the depletion zone to the bulk, while its location is pinned to the end of the depletion zone.

As an example, the hopping mechanism for R to S is shown in (**Figure 4**)a and b, for the equilibrium and non-equilibrium case, respectively. In equilibrium,  $\Delta G = 0$ , the effective migration barrier is the saddle point energy:

$$\Delta G_{\text{B,S}} \mid_{\Delta G = 0} = G_{\text{B0,S}} \tag{24}$$

In non-equilibrium the effective barrier is given by the modulated saddle point energy and the modulated energy at  $G_R$ :

$$\Delta G_{\text{B,S}} \mid_{\Delta G \neq 0, R \to S} = G_{\text{B,S}} - G_{\text{R}}$$
 (25)

 $G_{\rm B,S}$  is given by Equation (21). It consists of the equilibrium saddle point energy  $G_{\rm B0,S}$  modulated by  $\Delta G(a_{\rm STO},V,N)$ . Equally, we find a modulation of the energy at R,  $G_{\rm R}$ , at position 0.5 $a_{\rm STO}$ :

$$G_{\rm R} = G_{\rm R0} + \Delta G \left( 0.5 a_{\rm STO}, V, N \right)$$
 (26)

In Equation (26) the energy  $G_{R0}$  is the equilibrium energy at R. Using Equations (19) and (26), Equation (25) can be written as

$$\Delta G_{B,S} \mid_{\Delta G \neq 0, R \to S} = G_{B,S} - G_{R} = G_{B0,S} - G_{R0} + \{ \Delta G (a_{STO}, V, N) - \Delta G (0.5 a_{STO}, V, N) \}$$
(27)

For the hopping in the opposite direction, the energy at S must be considered, which is modulated by  $\Delta G(1.5a_{STO}, V, N)$ . The

ADVANCED ELECTRONIC MATERIALS

www.advelectronicmat.de

effective barrier is given by

$$\Delta G_{B,S} \mid_{\Delta G \neq 0, S \to R} = G_{B,S} - G_{S} = G_{B0,S} - G_{S0} + \{ \Delta G (a_{STO}, V, N) - \Delta G (1.5 a_{STO}, V, N) \}$$
(28)

The barrier is modulated by the superimposed energy  $\Delta G$ , which decreases over time as refilling continues. The modulation is determined by the position of the barrier with respect to the minimum of  $\Delta G$ . In other words, if the barrier lies in a region with a negative slope, the barrier is lowered, whereas a positive slope increases the effective barrier height with respect to the equilibrium value. Barriers on the left half with respect to the minimum are lowered, and barriers on the right are increased. As we will see in Section 4, these dynamics favor a fast incorporation.

The metal cannot be treated as an infinite reservoir of oxygen. Instead, the oxygen inside the metal is rather approximately the amount that was incorporated during the SET pulse. Besides the rate of oxygen transfer in the container and between the environments, there is a limit of free lattice spots in each layer. Here, this number is given by the equilibrium oxygen vacancy concentration  $N_{\rm HRS}$ . For  $N_{\rm A} \geq N_{\rm HRS}$  the amount of oxygen vacancies, which were created in a specific range A, are given by  $N_{\rm A}(t)-N_{\rm HRS}$ . This is equal to the number of oxygen ions which can be added to range A. This means an inflow of oxygen ions. In reverse, if the oxygen vacancy concentration falls below the HRS value,  $N_{\rm A}(t) < N_{\rm HRS}$ , the number of oxygen ions that can be removed is given by  $N_{\rm HRS}-N_{\rm A}(t)$ . This equals an outflow of oxygen. We can define the hopping probability P using Equation (19) as

$$P_{A\to B} = R_{AB} \times (N_B(t) - N_{HRS}) \tag{29}$$

As an example, the hopping probability from the metal to the recombination region  $P_{M \to R}$  is given by Equation (30):

$$P_{\mathrm{M}\to\mathrm{R}} = v_{\mathrm{Ph}} \exp\left(-\frac{G_{\mathrm{B,M}}\left(V,N\right) - G_{\mathrm{M}}\left(V,N\right)}{k_{\mathrm{B}}T}\right) \times \left(N_{\mathrm{R}}\left(t\right) - N_{\mathrm{HRS}}\right)$$
 (30)

The remaining transition probabilities are calculated using Equation (29) with the Gibbs barriers and energy barriers according to Equations (20)–(23), and Equations (14)–(18), respectively.

By defining all transitions between the environment and the three ranges with their corresponding neighbors allows to derive three coupled ordinary differential equations for each layer inside the depletion zone. The differential equation of the recombination layer R is given by Equation (31) and the supply layer S by Equation (32) and the transition layer T by Equation (33):

$$\frac{\mathrm{d}N_{\mathrm{R}}}{\mathrm{d}t} = \begin{cases} \left(R_{\mathrm{MR}} + R_{\mathrm{SR}}\right) \cdot \left(N_{\mathrm{R}} - N_{\mathrm{HRS}}\right) & N_{\mathrm{R}} \ge N_{\mathrm{HRS}} \\ \left(-R_{\mathrm{RM}} - R_{\mathrm{RS}}\right) \cdot \left(N_{\mathrm{HRS}} - N_{\mathrm{R}}\right) & N_{\mathrm{R}} < N_{\mathrm{HRS}} \end{cases}$$
(31)

$$\frac{\mathrm{d}N_{\mathrm{S}}}{\mathrm{d}t} = \begin{cases} \left(R_{\mathrm{RS}} + R_{\mathrm{BS}}\right) \cdot \left(N_{\mathrm{S}} - N_{\mathrm{HRS}}\right) & N_{\mathrm{S}} \ge N_{\mathrm{HRS}} \\ \left(-R_{\mathrm{SR}} - R_{\mathrm{SB}}\right) \cdot \left(N_{\mathrm{HRS}} - N_{\mathrm{S}}\right) & N_{\mathrm{S}} < N_{\mathrm{HRS}} \end{cases}$$
(32)

$$\frac{\mathrm{d}N_{\mathrm{T}}}{\mathrm{d}t} = \begin{cases} \left(R_{\mathrm{ST}} + R_{\mathrm{BT}}\right) \cdot \left(N_{\mathrm{T}} - N_{\mathrm{HRS}}\right) & N_{\mathrm{T}} \geq N_{\mathrm{HRS}} \\ \left(-R_{\mathrm{TS}} - R_{\mathrm{TB}}\right) \cdot \left(N_{\mathrm{HRS}} - N_{\mathrm{S}}\right) & N_{\mathrm{T}} < N_{\mathrm{HRS}} \end{cases}$$
(33)

The HRS concentration for the readout at  $V_{\rm Read}$  is fitted to the end of the decay current signal.

#### 4. Results and Discussion

In this section, we present the simulation results and apply the presented ionic model to our experimental data. The presented model was implemented in Julia and the differential equations were solved numerically using Julia's ODE package. [49] We apply the model to two cases. In the first, the device is fully switched applying a pulse of 3.5 V with a length of 10 ms. Here, fully switched refers to an LRS value of at least 1  $\mu A$ , which is three orders of magnitude higher than the HRS current. In the second case, it is only partially switched with a pulse of 3.5 V with a length of 0.5 ms. Each intermediate state is a superposition of these two cases. The readout voltage during the decay is 0.3 V in both cases. The initial conditions of the simulations are shown in Table 1. The parameters were fitted to our measurement data but are reasonably close to the values reported in the literature.

The oxygen vacancy concentrations and the filament radius  $r_{\rm filament}$  depend on the switching conditions, in particular on the pulse width. For this reason, we fit the initial concentration after the SET (LRS)  $N=N_{\rm LRS}$  and the radius of the filament, within a reasonable range, to the starting current of decay  $I_0$  as an initial condition. The specific barrier between the Pt electrode and the oxide is unknown since it depends strongly on the interface conditions. Zurhelle et al. calculated activation energies in the backward direction of 0.16 eV and 0.86 eV for an interstitial site in the Pt after a first jump and after a second jump, respectively. For a backward jump from a Pt vacancy, a value of 0.39 eV is given. [22]

In our simulation a STO bulk oxygen migration barrier of 0.82 eV is used as equilibrium value.  $G_{\rm B,S}$  is set to 0.74 eV to fit both cases equally. This is a sensible approach and will be explained later. The simulation model allows to calculate the oxygen vacancy concentration over time inside the depletion zone. The concentrations are mapped to the corresponding currents by the introduced Tsu-Esaki conduction mechanism, as described in Section 2.

#### 4.1. Simulation Result: Long SET Pulses

The simulation results in comparison to the experiment of the fully switched device are illustrated in (**Figure 5**)a. The device was switched to LRS applying a 3.5 V, 10 ms pulse to the top electrode with a measurement current compliance of 3 mA.

We assume that the three regions are completely depleted of oxygen during the voltage pulse. Thus, the same LRS vacancy concentration,  $1.94 \times 10^{27} \, \text{m}^{-3}$ , for R, S, and T are applied. Our model predicts the current decay over two orders of magnitude correctly within the correct time scale.

During the decay the depletion zone width increases from 1.3 nm to 3.0 nm, as shown in Figure 5b. The respective  $\Delta G$  values for the HRS and the LRS are illustrated in Figure 5c. The maximum  $\Delta G$  is  $\approx -0.7$  eV and occurs for the lowest LRS, hence, the highest oxygen vacancy concentration. For the simulation, the oxygen vacancy concentration for R, S, and T at the first-time step is  $N_{\rm LRS}=1.94\times10^{27}~{\rm m}^{-3}$  and after the last time step  $N_{\rm HRS}=3.66\times10^{26}~{\rm m}^{-3}$ . We used a filament width of 950 nm which is close to the experimental value observed in previous spectroscopy experiments.  $^{[17]}$  Figure 5d shows the equilibrium migration barriers. The other parameters are presented in Table 1.

conditions) on Wiley Online Library for rules of use; OA articles are governed by the applicable Creative Commons License

Table 1. Model parameters. The values were fitted to the measured data.

Parameter		Long SET Pulses	Short SET Pulses
Saddle point energy – B	G <sub>B0,B</sub> (eV)	0.8[11]	0.8[11]
Saddle point energy – T	$G_{\mathrm{B0,T}}(\mathrm{e}V)$	0.8[11]	0.8[11]
Saddle point energy – S	$G_{B0,S}(eV)$	0.73[11]	0.73[11]
Saddle point energy – M	$G_{BO,M}$ (eV)	0.8[11]	0.8[11]
Reference energy – Metal	G <sub>0</sub> (eV)	0.16	0.16
Reference energy – STO	G <sub>B,0</sub> (eV)	0 (reference)	0 (reference)
Oxygen vacancy concentration of R in LRS	$N_{\rm R,LRS}~(m^{-3})$	$1.94 \times 10^{27[32]}$	$1.83 \times 10^{27[32]}$
Oxygen vacancy concentration of S in LRS	$N_{\rm S,LRS}~(m^{-3})$	$1.94 \times 10^{27[32]}$	$1.23 \times 10^{27[32]}$
Oxygen vacancy concentration of T in LRS	$N_{T,LRS}~(m^{-3})$	$1.94 \times 10^{27[32]}$	$4.44 \times 10^{26[32]}$
Equilibrium concentration in HRS	$N_{\rm HRS}~(m^{-3})$	$3.6 \times 10^{26[32]}$	$2.9 \times 10^{26[32]}$
Oxide thickness	$t_{Ox}(nm)$	10	10
Filament radius	$r_{ m filament}$ (nm)	950 <sup>[17]</sup>	810 <sup>[17]</sup>
Built-in energy	$\psi_{Bi}$ (eV)	1.3 <sup>[33]</sup>	1.3 <sup>[33]</sup>
Dielectric constant	$\epsilon_r$	32 <sup>[50]</sup>	32 <sup>[50]</sup>
Lattice constant STO	a <sub>sto</sub> (m)	$3.9 \times 10^{-10[50]}$	$3.9 \times 10^{-10[50]}$
Phonon frequency	$v_{\rm Ph}~({\rm s}^{-1})$	$6 \times 10^{12[11]}$	$6 \times 10^{12[11]}$
Average number of unit cells located within T	A	2.5	2.5

The respective time evolution of the three state variables,  $N_{\rm R}$ ,  $N_{\rm S}$ , and  $N_{\rm T}$  and the transition rates R are shown (**Figure 6**)a and Figure 6b–i, respectively. At short time scales after the pulse, <100 ms, the concentration in R and S decreases strongly, which is governed by the high hopping rates from the metal M to the interface slab R, see Figure 6b. Here, the recombination rate is

determined by  $\Delta G_{\rm B,M}$ . Due to the non-equilibrium of the STO to its surroundings and the low oxygen migration barrier of 0.7 eV within the Pt, it is assumed to be constant during the decay process. This process explains the first sharp drop observed in the measurement. While oxygen incorporation continues, oxygen in S can migrate to the transition region, see Figure 6f. Since T is

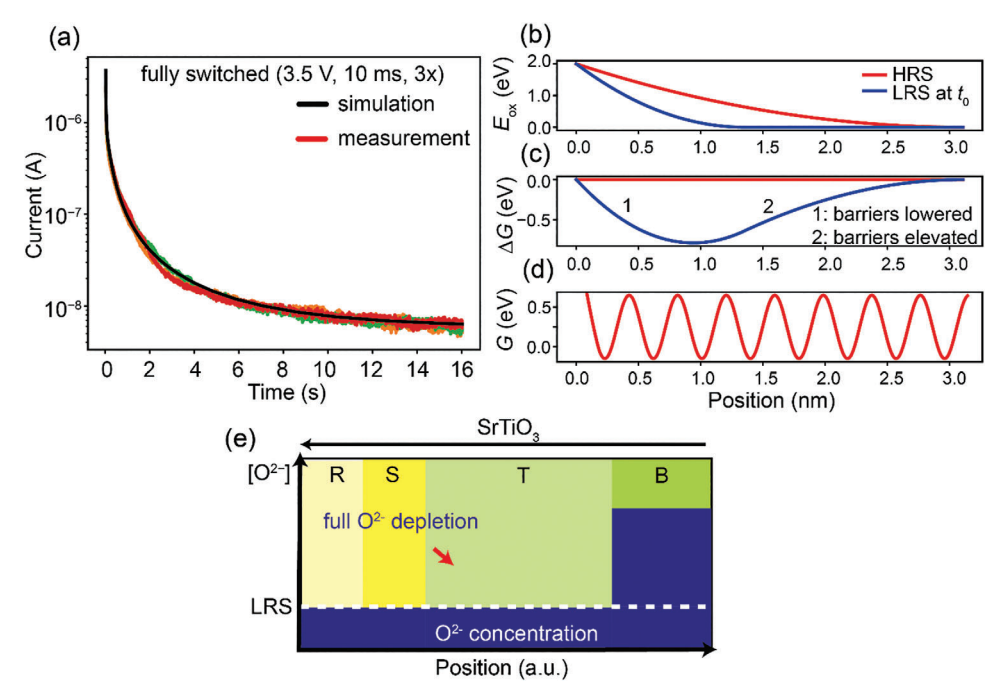
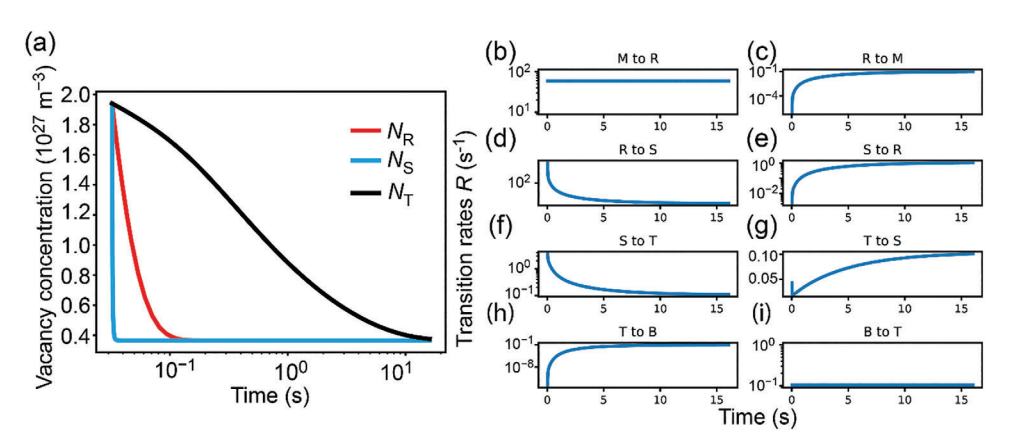


Figure 5. The measurement decay data for a switching pulse of  $3.5\,V$  and  $10\,ms$  for  $16\,s$  and the corresponding model results. a) The decay measurement is repeated three times. The simulation is shown as the black line. Fully switched refers to a fully depleted R, S, and T layer. b) The oxide energy at the interface shown for the LRS directly after the pulse (blue), and the equilibrium in the HRS (red). c) The deviation of the LRS oxide energy from the equilibrium. This is denoted as the  $\Delta G$ . d) The energy landscape in equilibrium without barrier height modulation. e) The oxygen ion concentration within the STO after the pulse for the fully switched device.

2199160x, 2024, 12, Downloaded from https://onlinelibrary.wiley.com/doi/10.1002/aclm.202400062 by Forschungszentrum Jülich GmbH Research Center, Wiley Online Library on [18/12/2024]. See the Terms and Conditions (https://onlinelibrary.wiley

com/terms-and-conditions) on Wiley Online Library for rules of use; OA articles are governed by the applicable Creative Commons



**Figure 6.** The oxygen vacancy concentration and their corresponding change per time during the decay process for the different regions for a device switched with a long pulse. a) The oxygen vacancy concentration in the depletion region for the recombination region  $N_R$  and for the supply region  $N_S$ . b–i) The ion hopping rates between the metal M, the recombination region R, the supply region S, the transition region T, and the bulk B for 16 s. The curves correspond to the simulation results shown in Figure 5.

located deeper inside the depletion zone, the refill lasts for the whole 16 s and determines the decay in the long term. The long term is mediated by  $\Delta G_{\rm B,T}$ , which approaches the bulk migration barrier of 0.82 eV over time. The negative slope of  $\Delta G$  left to the minimum, as shown in Figure 5c, lowers the effective barrier between R and S, and S and T, initially. This results in a high hopping rate from R to S and to T, while R is refilled. It quickly slows down as  $\Delta G$  is diminished, and equilibrium conditions are restored. It is interesting to note, that  $N_{\rm S}$  reaches the HRS value before  $N_{\rm R}$ . This indicates that the transport of oxygen away from the interface is faster than its reincorporation. With increasing oxygen in R, an increasing backflow of oxygen can be observed. Due to the positive slope in  $\Delta G$ , barriers on the right side of the minimum are increased. In our simulations this shows as an initial bulk exchange, T to B, of  $<10^{-9}~{\rm s}^{-1}$ .

#### 4.2. Simulation Result: Short SET Pulses

(**Figure 7**) shows the simulation results and the experimental data for the case of a 0.5 ms pulse with 3.5 V, twenty times shorter than the long pulse experiment.

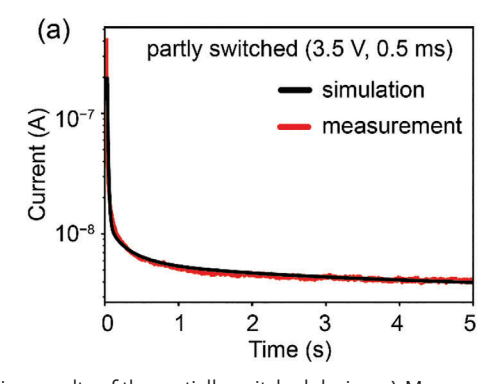
Here, the migration barriers remain the same, and only the oxygen vacancy concentration distribution is changed (It should

be noted that the depletion zone is still calculated using the average oxygen vacancy distribution N). The oxygen concentration after the voltage pulse is shown in Figure 7b. We assumed only a full depletion of the R region, and a partial depletion of the S region and the T region. Therefore,  $N_{\rm S}$  is set to 70% and  $N_{\rm T}$  to 23% of the LRS. An oxygen vacancy concentration in LRS of  $N_{\rm LRS}=1.82\times 10^{27}{\rm m}^{-3}$  was used. This starting condition leads to a decay in current very similar to our experimental observations. Figure 8aa shows the time evolution of the state variables. The decay is determined by the refill of  $N_{\rm R}$  and  $N_{\rm S}$ . The hopping rates give a similar picture compared to the long pulse experiment, as shown in Figure 8b–i.

Compared to the experiments with the long pulses, the device has decayed back to the HRS once R is refilled. This is the result of the fast oxygen incorporation into the recombination zone. Our simulation shows very little bulk activation, which is indicated by an almost complete loss of the LRS state within the first 200 ms.

#### 4.3. Discussion

Overall, the model and previous studies indicate that the current decay is a complex process depending on the parameter set, the migration within the top electrode, the interface transition, and



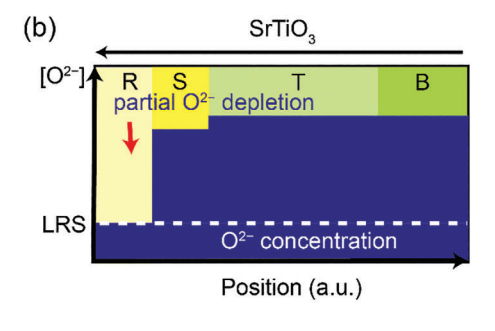


**Figure 7.** Simulation results of the partially switched device. a) Measurement data for a short voltage pulse and the corresponding simulation results. The simulation indicates a strong activation of the recombination region, with only very little supply region. b) The oxygen ion concentration (blue) within the STO after the pulse for the partially switched device.



www.advelectronicmat.de

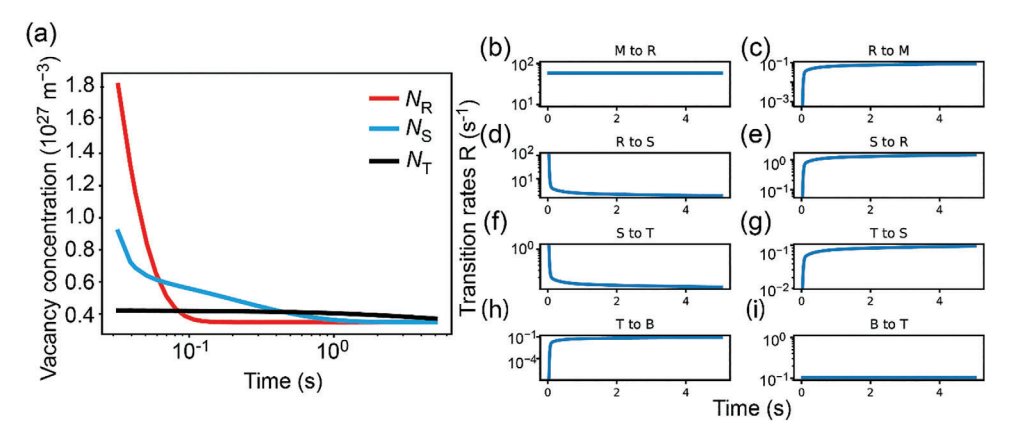


**Figure 8.** The simulated oxygen vacancy concentration and their corresponding change per time during the decay process for the different regions for a device switched with a short pulse. a) The oxygen vacancy concentration in the depletion region for the recombination region  $N_R$ . and for the supply region  $N_S$ . b) The ion hopping rates between the metal M, the recombination region R, the supply region S and the bulk B for 16 s. The curves correspond to the simulation results shown in Figure 7.

the ion migration near the surface. We show that the decay after switching the device to the LRS is determined by the deviation from equilibrium, specifically  $\Delta G$ , that has been created. Saddle points located to the left of the minimum of  $\Delta G$  are lowered favoring a rapid reoxidation of the filament directly at the interface. In contrast, the ones to the right are initially raised resulting in an initial low bulk contribution and a rapid refill of slabs close to the Pt interface. This behavior is reflected in the hopping rates, see Figures 6 and 8, which reflect the transient barrier modulation  $\Delta G$ . The barriers in the left branch are initially very low and quickly saturate. In our model we have a barrier on the right connecting the depletion zone to the bulk. This barrier initially shows a low hopping rate but increases as T refills and the barrier distortion decreases. As the barrier relaxes back to the HRS equilibrium, the minimum of  $\Delta G$  shifts to the right while the total  $\Delta G$  decreases. In this way the barriers are activated in the second half. As the first slabs are refilled, the decay is determined by the filling of slabs located close to the end of the depletion zone. In our simulation the S slab is filled faster than the R slab. This pass-forward effect is due to the low migration barrier of S, which does not have an equilibrium height of 0.82 eV like  $G_{\rm B,T}$ and  $G_{\rm B,B}$ . The migration barrier  $G_{\rm B,S}$  in equilibrium is  $\approx 0.73$  eV in our model to fit the measurement for the short pulse and the long pulse simultaneously. This may indicate that we either have lattice distortions at the interface causing the migration barrier to shrink, [51] or that the slope of  $\Delta G$  is more negative than in our calculations. This may be the result of a non-homogeneous oxygen vacancy distribution within the depletion zone, as observed in experiments, but was approximated to be homogenous in this study for simplicity.

#### 5. Conclusion

In conclusion, our discussion shows that the decay observed in 8w-switching STO ReRAM cells is likely to be the result of ionic reoxidation and not associated with electron trapping. Electron trapping can be ruled out because either the corresponding time constants are too small or the resulting currents flow in the opposite direction as observed in our measurements. We propose an

ionic model that is consistent with our previous studies. Here the decay is the result of reoxidation of the interfacial region within the depletion zone. This process is driven by the chemical potential gradient created during the SET process to the LRS from the equilibrium HRS state. The oxygen migration barriers for the interface transition and inside the STO at the vicinity of the Pt interface are modulated by the interface energy. Our model shows that the milliseconds time constants directly after the pulse can be attributed to the rapid incorporation of oxygen into the first slabs. The intermediate time constants are determined by the superposition of several migration barriers resulting from the distortion of the Gibbs free energy by the depletion zone and the strong concentration gradient. Longer time constants (second range) indicate a bulk activation, where the rate-determining step is the ionic hopping inside the STO lattice.

This work allows the identification of possible parameters to tune the relaxation process of 8w-switching STO ReRAM cells. The decay can be roughly divided into two parts. On the one hand, there is the supply of oxygen from the electrode and, on the other hand, the oxygen vacancy resupply from the bulk or supply region. The reincorporation of oxygen into the STO is mediated by an activation energy. By controlling this activation energy, the reoxidation rate of oxygen vacancies in the recombination zone, and hence the sharp drop immediately after the SET pulse, could be manipulated. In the long term, the resupply of oxygen vacancies is determined by the bulk ion migration barrier of the STO. This barrier can be modified by strain and stoichiometry engineering. [51,52]

The model can be used to understand both volatile and non-volatile behavior of VCM cells. The interfacial and bulk migration barriers can be adjusted to account for different oxides, electrodes or additional oxygen blocking interlayers. Devices with high time constants arising from oxygen blocking interlayers or a higher bulk oxygen migration barrier can be simulated by using a high migration barrier at the interface or within the bulk, respectively.

Our work can be extended to other VCM systems where ionic exchange between different interfaces is the origin of resistive switching. The 8w-switching mechanism is determined by an oxygen exchange between an oxide and a metal. This

2199160x, 2024, 12, Downloaded from https://onlinelibrary.wiley.com/doi/10.1002/aclm.202400062 by Forschungszentrum Jülich GmbH Research Center, Wiley Online Library on [18/1/22024]. See the Terms and Conditions (https://onlinelibrary.wiley.com/doi/10.1002/aclm.202400062 by Forschungszentrum Jülich GmbH Research Center, Wiley Online Library on [18/1/22024]. See the Terms and Conditions (https://onlinelibrary.wiley.com/doi/10.1002/aclm.202400062 by Forschungszentrum Jülich GmbH Research Center, Wiley Online Library on [18/1/22024]. See the Terms and Conditions (https://onlinelibrary.wiley.com/doi/10.1002/aclm.202400062 by Forschungszentrum Jülich GmbH Research Center, Wiley Online Library on [18/1/22024]. See the Terms and Conditions (https://onlinelibrary.wiley.com/doi/10.1002/aclm.202400062 by Forschungszentrum Jülich GmbH Research Center, Wiley Online Library on [18/1/22024]. See the Terms and Conditions (https://onlinelibrary.wiley.com/doi/10.1002/aclm.202400062 by Forschungszentrum Jülich GmbH Research Center, Wiley Online Library.

conditions) on Wiley Online Library for rules of use; OA articles are governed by the applicable Creative Commons

www.advancedsciencenews.com

www.advelectronicmat.de

mechanism has been observed in several systems, such as  ${\rm Ta_2O_5}$ ,  ${}^{[53]}$   ${\rm TiO_2}$ ,  ${}^{[54]}{\rm NiO}$ ,  ${}^{[55]}$   ${\rm CeO_2}$ . Furthermore, the concepts presented are also valid for ionic exchange between interlayers, especially when these layers have different work functions and interface energies.

## 6. Experimental Section

A 10 nm thick STO was grown on a (100) single crystal Nb:STO (0.5 wt%) substrate by pulsed laser deposition, followed by electron beam evaporation of the Pt top electrode. The top electrode Pt layer was embedded in an insulator and contacted with a gold lead. The sample preparation could be extracted from Siegel et al. [56] Pulse measurements were performed using the Pulse Measurement Units (PMU) of the Keithley 4200 SCA. The current was measured through the bottom electrode to exclude capacitive charging of the measurement equipment (cables). A current range of 1  $\mu\text{A}$  was used. During pulse experiments, a current compliance of 3 mA was given by the measurement resistance of  $R_{\text{meas}}$ . Current–voltage curves were measured using a Keithley 2400.

# **Supporting Information**

Supporting Information is available from the Wiley Online Library or from the author.

# Acknowledgements

Funded by the Deutsche Forschungsgemeinschaft (DFG, German Research Foundation) — Project MemTDE Project number 441959088 as part of the DFG priority program SPP 2262 MemrisTec — Project number 422738993. DS received funding from the EU Horizon 2020 program under the MSCA—ITN action MANIC, grant agreement No 861153. AS and CF acknowledge for funding by the Federal Ministry of Education and Research project NEUROTEC (Grants No. 16ME0398K and No. 16ME0399).

#### **Conflict of Interest**

The authors declare no conflict of interest.

#### **Data Availability Statement**

The data that support the findings of this study are available from the corresponding author upon reasonable request.

#### **Keywords**

memristive device, retention, VCM

Received: January 30, 2024 Revised: April 19, 2024 Published online: June 17, 2024

- [1] D. Markovic, A. Mizrahi, D. Querlioz, J. Grollier, Nat Rev Phys 2020, 2, 499.
- [2] S. O. Park, H. Jeong, J. Park, J. Bae, S. Choi, Nat. Commun. 2022, 13, 2888.

- [3] R. Berdan, E. Vasilaki, A. Khiat, G. Indiveri, A. Serb, Sci. Rep. 2016, 6, 18639.
- [4] T. Chang, S.-H. Jo, K.-H. Kim, P. Sheridan, S. Gaba, W. Lu, Appl. Phys. A: Mater. Sci. Process. 2011, 102, 857.
- [5] S. Fukuyama, K. Maeda, S. Matsuda, K. Takeuchi, R. Yasuhara, presented at IEEE Int. Reliab. Phys. Symp. Proc Burlingame, CA, USA, March, 2018.
- [6] E. Wu, T. Ando, Y. Kim, R. Muralidhar, E. Cartier, P. Jamison, M. Wang, V. Narayanan, 2019 IEEE Int. Electron Devices Meeting, San Francisco, CA, USA, Dec. 2019.
- [7] G. Zhou, Z. Wang, B. Sun, F. Zhou, L. Sun, H. Zhao, X. Hu, X. Peng, J. Yan, H. Wang, W. Wang, J. Li, B. Yan, D. Kuang, Y. Wang, L. Wang, S. Duan, Adv. Electron. Mater. 2022, 8, 2101127.
- [8] T. Chang, S. Jo, W. Lu, ACS Nano 2011, 5, 7669.
- [9] R. Dittmann, S. Menzel, R. Waser, Adv. Phys. 2022, 70, 155.
- [10] C. Funck, S. Menzel, ACS Appl. Electron. Mater. 2021, 3, 3674.
- [11] R. A. De Souza, Adv. Funct. Mater. 2015, 25, 6326.
- [12] R. Merkle, J. Maier, Angew. Chem., Int. Ed. 2008, 47, 3874.
- [13] C. Funck, C. Bäumer, S. Wiefels, T. Hennen, R. Waser, S. Hoffmann-Eifert, R. Dittmann, S. Menzel, Phys. Rev. B 2020, 102, 035307.
- [14] R. De Souza, Curr. Opin. Solid State Mater. Sci. 2021, 25, 100923.
- [15] C. Baeumer, N. Raab, T. Menke, C. Schmitz, R. Rosezin, P. M. Müller, M. Andrä, V. Feyer, R. Bruchhaus, F. Gunkel, C. M. Schneider, R. Waser, R. Dittmann, *Nanoscale* 2016, 8, 13967.
- [16] M. B. Milde, O. J. N. Bertrand, H. Ramachandran, M. Egelhaaf, E. Chicca, Neural Comput 2018, 30, 2384.
- [17] D. Cooper, C. Baeumer, N. Bernier, A. Marchewka, C. La Torre, R. E. Dunin-Borkowski, S. Menzel, R. Waser, R. Dittmann, Adv. Mater. 2017. 29, 1700212.
- [18] C. Baeumer, C. Schmitz, A. H. H. Ramadan, H. Du, K. Skaja, V. Feyer, P. Muller, B. Arndt, C. Jia, J. Mayer, R. A. De Souza, C. M. Schneider, R. Waser, R. Dittmann, *Nat. Commun.* 2015, 6, 9610.
- [19] F. V. E. Hensling, T. Heisig, N. Raab, C. Baeumer, R. Dittmann, Solid State Ionics 2018, 325, 247.
- [20] N. Raab, C. Bäumer, R. Dittmann, AIP Adv. 2015, 5, 047150.
- [21] J. Xiong, R. Yang, J. Shaibo, H. M. Huang, H. K. He, W. Zhou, X. Guo, Adv. Funct. Mater. 2019, 29, 1807316.
- [22] A. Zurhelle, PhD Thesis, RWTH Aachen, 2023.
- [23] F. Nie, J. Wang, H. Fang, S. Ma, F. Wu, W. Zhao, S. Wei, Y. Wang, Le Zhao, S. Y., Mater. Futures 2023, 2, 035302.
- [24] H. Li, S. Geng, T. Liu, M. Cao, J. Su, ACS Appl. Mater. Interfaces 2023, 15, 5456.
- [25] C. Giotis, A. Serb, S. Stathopoulos, L. Michalas, A. Khiat, T. Prodromakis, IEEE Trans. Electron Devices 2020, 67, 5158.
- [26] E. Mikheev, B. D. Hoskins, D. B. Strukov, S. Stemmer, *Nat. Commun.* 2014, 5, 3990.
- [27] Q. Wang, D. He, Sci. Rep. 2017, 7, 822.
- [28] E. M. Bourim, Y. Kim, D. W. Kim, ECS J. Solid State Sci. Technol. 2014, 3, N95.
- [29] D. J. Seong, M. Jo, D. Lee, H. Hwang, Electrochem. Solid-State Lett. 2007, 10, H168.
- [30] B. Zhao, M. Xiao, Y. N. Zhou, Nanotechnology 2019, 30, 425202.
- [31] C. Du, W. Ma, T. Chang, P. Sheridan, W. D. Lu, Adv. Funct. Mater. 2015, 25, 4290.
- [32] C. Baeumer, C. Schmitz, A. Marchewka, D. N. Mueller, R. Valenta, J. Hackl, N. Raab, S. P. Rogers, M. I. Khan, S. Nemsak, M. Shim, S. Menzel, C. M. Schneider, R. Waser, R. Dittmann, *Nat. Commun.* 2016, 7, 12398.
- [33] C. Baeumer, C. Funck, A. Locatelli, T. O. Mente, F. Genuzio, T. Heisig, F. Hensling, N. Raab, C. M. Schneider, S. Menzel, R. Waser, R. Dittmann, Nano Lett. 2019, 19, 54.
- [34] I. Isakov, M. J. L. Sourribes, P. A. Warburton, J. Appl. Phys. 2017, 122, 94305.



ADVANCED ELECTRONIC MATERIALS

www.advelectronicmat.de

- [35] M. S. Tyagi, Met.-Semicond. Schottky Barrier Junctions Their Appl, (Ed: B.L. Sharma), Springer, Boston, MA 1984.
- [36] G. Wentzel, Z Med Phys 1926, 38, 518.
- [37] A. Marchewka, B. Roesgen, K. Skaja, H. Du, C. L. Jia, J. Mayer, V. Rana, R. Waser, S. Menzel, Adv. Electron. Mater. 2016, 2, 1500233.
- [38] R. Tsu, L. Esaki, Appl. Phys. Lett. 1973, 22, 562.
- [39] T. Heisig, C. Baeumer, U. N. Gries, M. P. Mueller, C. La Torre, M. Luebben, N. Raab, H. Du, S. Menzel, D. N. Mueller, C.-L. Jia, J. Mayer, R. Waser, I. Valov, R. A. De Souza, R. Dittmann, Adv. Mater. 2018, 30, 1800957.
- [40] D. K. Schroder, Defects, in Semiconductor Material and Device Characterization (Eds.), IEEE 2006, 251.
- [41] D. Cho, K. Kim, K. Lee, M. Lübben, S. Chen, I. Valov, ACS Appl. Mater. Interfaces 2023, 15, 18528.
- [42] A. F. Zurhelle, W. Stehling, R. Waser, R. A. De Souza, S. Menzel, Adv. Mater. Interfaces 2022, 9, 2101257.
- [43] R. A. De Souza, V. Metlenko, D. Park, T. E. Weirich, Phys. Rev. B 2012, 85, 174109.
- [44] J. Maier, J. Maier, Z. Phys. Chemie-Int. J. Res. Phys. Chem. Chem. Phy 2005, 219, 35.
- [45] In this work  $\Delta G$  refers to the deviation of the local Gibbs free energy from equilibrium arising from the SET process, whereas the indexed  $\Delta GB$ , i refers to the effective oxygen migration barrier at a specific position.

- [46] A. R. Genreith-Schriever, R. A. De Souza, Phys. Rev. B 2016, 94, 224304.
- [47] S. Dirkmann, M. Hansen, M. Ziegler, H. Kohlstedt, T. Mussenbrock, Sci. Rep. 2016, 6, 35606.
- [48] S. Menzel, U. Böttger, M. Wimmer, M. Salinga, Adv. Funct. Mater. 2015, 25, 6306.
- [49] C. Rackauckas, Q. Nie, J. Open Res. Software 2017, 5.
- [50] J. Kim, L. Kim, D. Jung, I. Kim, J. Je, J. Lee, Ferroelectrics 2005, 327, 103.
- [51] H. Dou, M. Hellenbrand, M. Xiao, Z. Hu, S. Kunwar, A. Chen, J. L. MacManus-Driscoll, Q. Jia, H. Wang, Adv. Electron. Mater. 2023, 9, 2201186.
- [52] L. Iglesias, A. Sarantopoulos, C. Magen, F. Rivadulla, Phys. Rev. B 2017, 95, 165138.
- [53] A. Schönhals, C. M. M. Rosario, S. Hoffmann-Eifert, R. Waser, S. Menzel, D. J. Wouters, Adv. Electron. Mater. 2017, 4, 1700243.
- [54] N. Xiao, M. A. Villena, B. Yuan, S. Chen, B. Wang, M. Eliáš, Y. Shi, F. Hui, X. Jing, A. Scheuermann, K. Tang, P. C. McIntyre, M. Lanza, Adv. Funct. Mater. 2017, 27, 1700384.
- [55] M. Zhao, Y. Zhu, Q. Wang, M. Wei, X. Liu, F. Zhang, C. Hu, T. Zhang, D. Qiu, M. Li, R. Xiong, Appl. Phys. Lett. 2016, 109, 13504.
- [56] S. Siegel, C. Baeumer, A. Gutsche, M. von Witzleben, R. Waser, S. Menzel, R. Dittmann, Adv. Electron. Mater. 2021, 7, 2000815.